Available online at www.sciencedirect.com
SciVerse ScienceDirect
Acta Materialia 61 (2013) 4329–4338
Acta MATERIALIA
www.elsevier.com/locate/actamat

The dependence of shear modulus on dynamic relaxation and evolution of local structural heterogeneity in a metallic glass

L.S. Huo [a,b], J.F. Zeng [a], W.H. Wang [b,*], C.T. Liu [a], Y. Yang [a,*]

[a] Centre for Advanced Structural Materials, Department of Mechanical and Biomedical Engineering, City University of Hong Kong, Tat Chee Avenue, Kowloon Tong, Kowloon, Hong Kong, People's Republic of China
[b] Institute of Physics, Chinese Academy of Sciences, Beijing 100190, People's Republic of China

Received 29 March 2013; received in revised form 1 April 2013; accepted 3 April 2013
Available online 3 May 2013

Abstract

Starting from the nanoscale structural heterogeneities intrinsic to metallic glasses (MGs), here we show that there are two concurrent contributions to their microscale quasi-static shear modulus G_I: one (μ) is related to the atomic bonding strength of solid-like regions and the other (G_{II}) to the change in the possible configurations of liquid-like regions (dynamic relaxation). Through carefully designed high-rate nanoscale indentation tests, a simple constitutive relation ($\mu = G_I + G_{II}$) is experimentally verified. On a fundamental level, our current work provides a structure–property correlation that may be applicable to a wide range of glassy materials.

Keywords: Metallic glass; Elastic modulus; Structural heterogeneity; Nanoindentation

1. Introduction

Owing to their unique combination of mechanical/physical properties, metallic glasses (MGs) are considered to be excellent candidate materials for structural and functional use [1–6]. The great efforts dedicated to this field over the past decades have revealed that many important attributes of MGs, e.g. glass formation temperature, fragility, plasticity, etc., can be correlated with their elastic properties. The existence of these correlations is useful for the development of new MGs [7,8]; however, on a fundamental level, it is still not clear how the elastic properties of MGs can be correlated with so many important attributes, even including those related to plasticity. In general, it is known that the elastic moduli of solids are derived mainly from two factors: their atomic bonding strength and the possible relaxation spectra of their atomic structure. In crystals, the effect of the former usually overwhelms that of the latter at low temperatures; therefore, the quasi-static elastic moduli of crystalline materials are mainly related to their atomic bonding strength. By comparison, the shear moduli of MGs depend on not only atomic bonding strength but also structural relaxation. For example, previous experiments demonstrated that the shear modulus in a MG alloy was very sensitive to its thermo history, which could increase by ~30% after crystallization [8–12]. Furthermore, the prior atomistic simulations and experiments also showed that, even at low temperature, the elastic moduli of MGs are still affected by the stress-induced configurational change in their amorphous structure [13–16]. These previous findings suggest that, under a mechanical loading or thermal treatment, structural relaxation, as related to the configurational variation in an amorphous structure, could play an important role in determining the elastic moduli of MGs.

Recently, a number of experiments [17–20], consistent with many prior numerical simulations [13–15,21], have indicated that the structure of MGs is intrinsically heterogeneous in a dynamic sense, comprising liquid- and solid-like regions at the nanoscale. In general, one may envisage that, under a mechanical perturbation, the total deformation in

* Corresponding authors.
E-mail addresses: whw@iphy.ac.cn (W.H. Wang), yonyang@cityu.edu.hk (Y. Yang).

1359-6454/$36.00
http://dx.doi.org/10.1016/j.actamat.2013.04.004

an amorphous structure polarizes into the affine deformation in the solid-like regions and the non-affine deformation in the liquid-like ones [13–15]. Before the occurrence of overall yielding, the interplay between the two regions leads to an anelastic response of MGs which can be rationalized by a "core–shell" concept [17,19,20,22–25], as shown in Fig. 1. Here, it should be emphasized that the core–shell terminology currently used should not be misunderstood as that for a real composite material. In reality, there is no physical boundary that can be detected a priori for either the core or shell region in an amorphous structure which essentially has a continuous distribution of atomic packing. However, the notion of the core–shell structure is appealing to theoretical modeling, as seen below, and also useful for picturing the topological relation between the regions undergoing different types of deformations (affine vs. non-affine).

Despite the lack of a well-defined physical boundary, the "core" region may be loosely interpreted as the group of atoms exhibiting a lower packing density [26,27], a lower local modulus [28] or a higher energy dissipation rate [18,20,29] than those in the "shell" region [17,18,28]. Under a mechanical stress, the liquid-like cores may "evolve" many times by altering their configurations, which, however, does not immediately cause the overall yielding of a MG if the elastic shells are still interconnected [19,29]. This contrasts the original "shear transformation zone (STZ)" model [26], in which it was assumed that yielding is triggered once the liquid-like region transforms irreversibly. Following the core–shell concept, a dynamic structural evolution process can be conceived for MGs which entails many subcritical activation events in the apparent "elastic" deformation regime as centered in the different liquid-like cores. In this paper, we would like to show that, based on this kind of understanding of structural heterogeneity, i.e. the solid-/liquid-like regions [13–15,17–21,23,25], we can arrive at a simple constitutive relation that is able to correlate this nanoscale relaxation dynamics with the microscale "quasi-static" shear modulus.

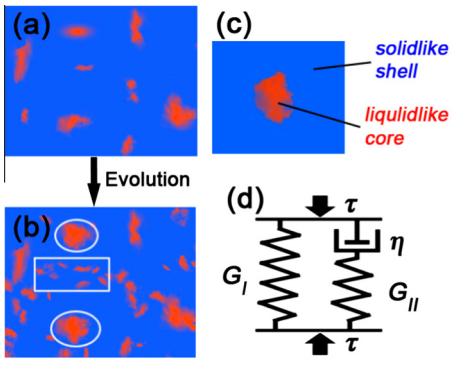

Fig. 1. (a) Schematic illustration of the zones of local heterogeneity being activated under stress in MGs (the red regions represent the liquid-like cores and the blue surroundings the elastic matrix); (b) illustration of the evolution of the structural heterogeneity; (c) sketch of the core–shell deformation unit in MGs; and (d) the three-parameter viscoelastic model derived according to Eq. (2). (For interpretation of the references to colour in this figure legend, the reader is referred to the web version of this article.)

2. Theory

2.1. Statistical shear transformation (SST) in the core–shell model

In principle, there could be two possible structural evolution routes for the configurational transition in the liquid-like cores, which are induced by an external stress in the apparent "elastic" deformation regime. As shown in Fig. 1a and b, one is due to the expansion of the existing liquid-like cores (the circle region in Fig. 1b) and the other to the successive activation of new cores (the rectangle region in Fig. 1b). Whichever route is followed, however, the overall effect of the structural evolution on a MG can be idealized as that on the core–shell structural model from a mean-field perspective, as shown in Fig. 1c. When subjected to a shear stress τ, the probability, p, of the liquid-like core transiting from one configuration to another without raising the total energy of the system can be derived as [29]:

$$\frac{dp}{dt} + 2\omega p e^{-\frac{\Delta G}{kT}} = 2\omega e^{-\frac{\Delta G}{kT}} \frac{\tau\Omega}{kT}, \tag{1}$$

where ω and ΔG denote the attempt frequency and energy barrier of the core configurational transition, respectively, t is the time, k the Boltzmann constant, T the ambient temperature, and Ω the activation volume for the configurational transition event. Now that the total strain γ of the core–shell structure depends on both the elastic (γ_e in the "shell") and inelastic (γ_i in the "core") strain, it can be generally written as $\gamma = \gamma(\gamma_e, \gamma_i)$. Here $\gamma_e = \tau/\mu$ with μ the shell's shear modulus, and $\gamma_i = \int d\gamma_i$ with $d\gamma_i$ the incremental inelastic strain and scaling with the transition probability $d\gamma_i \sim p$ [29]. Through the Taylor expansion, one can obtain a linear relation for the above strains, which is $\gamma \approx \gamma_e + \beta d\gamma_i$ or $\gamma \approx \tau/\mu + \beta p$, where the partial derivative $\beta = \partial\gamma/\partial\gamma_i$ measures the sensitivity of the total strain γ to its inelastic strain component γ_i. Substituting the above derivation into Eq. (1), we obtain:

$$\dot{\gamma} + 2\omega e^{-\frac{\Delta G}{kT}}\gamma = \frac{\dot{\tau}}{\mu} + 2\omega e^{-\frac{\Delta G}{kT}}\left(\frac{\beta\Omega}{kT} + \frac{1}{\mu}\right)\tau. \tag{2}$$

Now we obtain the constitutive relation, by taking the local shear transformation in the apparent "elastic" regime as a statistic activation process, which relates the applied shear stress τ and stress rate $\dot{\tau}$ to the resultant shear strain γ and strain rate $\dot{\gamma}$ in a MG. Note that if the energy barrier of the configurational transition is very high such that $\Delta G \gg kT$, these activation events could be severely suppressed ($e^{-\frac{\Delta G}{kT}} \sim 0$) and, in such a case, Eq. (2) is simplified to $\dot{\gamma} = \frac{\dot{\tau}}{\mu}$, the commonly used relation for linear elastic solids.

To help reveal the physical significance of the different terms in Eq. (2), it is worth mentioning that Eq. (2) is of

the same form as the constitutive relation for a phenomenological three-parameter viscoelastic model, as shown in Fig. 1d, which comprises a spring and a Maxwell unit connected in parallel [30]:

$$\dot{\gamma} + \frac{G_I G_{II}}{\eta(G_I + G_{II})}\gamma = \frac{\dot{\tau}}{G_I + G_{II}} + \frac{G_{II}}{\eta(G_I + G_{II})}\tau, \quad (3)$$

where G_I and G_{II} denote, respectively, the shear modulus of the springs connected in parallel and series with the dashpot with a viscosity η. Since Eqs. (2) and (3) are identical, we have $G_{II} = \alpha\mu/(1+\alpha)$, $G_I = \mu/(1+\alpha)$, $\eta = \frac{\alpha\mu}{2\omega e^{-\Delta G/kT}\cdot(1+\alpha)^2}$ and $\alpha = \beta\Omega\mu/(\mathrm{kT})$. Here $\alpha = \beta\Omega\mu/(kT)$ can be viewed as a factor embodying the total effect of the aggregated liquid-like cores, which increases with either the activation volume Ω or the sensitivity factor β. Here, it is worth mentioning that if α approaches infinity implicative of a completely "liquidized" amorphous structure with broken elastic shells, the three-parameter viscoelastic model would degenerate to the Maxwell model, which is the rheological model commonly accepted for supercooled metallic liquids [31]; on the other hand, if α approaches zero, symbolizing a fully "solidified" amorphous structure without any liquid-like cores, the three-parameter viscoelastic model would degenerate to an elastic spring model. In that regard, the amorphous structure for the general case of a finite α can be viewed as a "solid–liquid" composite owing to its mixed viscoelastic response.

2.2. Configurational (entropic) dependence of shear modulus

Note that the above expressions for G_I, G_{II} and η could have many important physical implications. However, what we are interested in here is to explore the physical meaning of G_I, the quasi-static shear modulus obtained at $\dot{\gamma} \sim 0$. Through the rearrangement of the above expressions, one can easily obtain a simple but rather intriguing relation:

$$G_I = \mu - G_{II}. \quad (4)$$

Here G_{II} represents a "modulus" inherited mainly from the liquid-like cores, which attains its maximum as α approaches infinity. In principle, for the same G_I, there could be many possible combinations of μ and G_{II}. Note that Cheng and Ma derived a similar relation based on thermodynamics in 2009 [13], which may be written as $G_I = G_p + G_k - G_e$. In this relation, G_p, G_k and G_e are all positive numbers and represent the shear modulus derived from the atomic potential, the atom kinetic energy and the configurational entropy of the glassy system, respectively. Through atomistic simulations, they further found that G_k is negligibly small as compared to G_p and G_e [13]. In such a case, we have $G_I \cong G_p - G_e$. Comparing this relation with Eq. (4), one can recognize that, if taking $\mu = G_p$ and $G_{II} = G_e$, the constitutive relation herein derived, which is based on the concept of the statistical shear transformation (SST) in an elastic shell, is equivalent to that derived based on thermodynamics [13]. In other words, the shear modulus due to the atomic potential, G_p, as defined in Cheng's work [13], can be ascribed to the atomic bonding in the elastic shells, and the shear modulus due to the configurational entropy, G_e, can be related to the enumeration of the possible configurations of the liquid-like cores. Therefore, from a theoretical viewpoint, the prediction of our micromechanical modeling finds good agreement with the prior atomistic simulations and thermodynamic theory. Next, we would like to carry out experiments to directly verify the above constitutive relation. Furthermore, if the relation could be verified, we would like to address the following important questions: (i) what is the appropriate value for μ? And (ii) how do G_I or G_{II} vary with the external stimuli, such as stress or temperature, in line with the change in the volume fraction of the liquid-like cores in a MG alloy?

3. Experiment

To verify the above constitutive relations experimentally, we employed a spherical indentation approach featuring an asymmetric loading–holding–unloading profile,

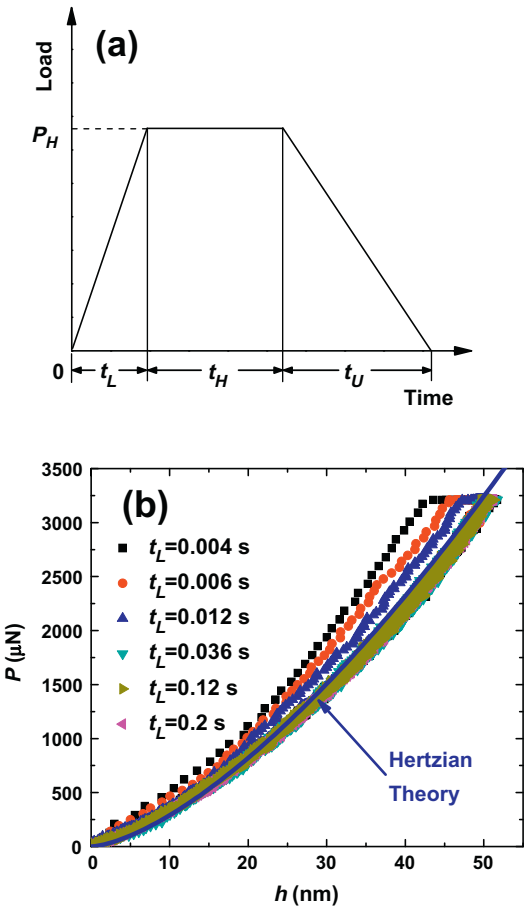

Fig. 2. (a) Sketch of the indentation load function, and (b) representative nanoindentation P–h curves obtained at $P_H = 3200$ μN, showing the anelastic deformation in the MG. Note that the Hertzian curve corresponds to the indenter tip radius of 5 μm, shear modulus (31 GPa) and Poisson's ratio (0.363) of Vit105.

Table 1
The calculated parameters in the anelastic model for Vit105 MG at different loads. The G_{II} and $\beta\Omega$ at the four lower loads (in parentheses) are calculated according to $G_I = \mu - G_{II}$ and $G_{II} = \alpha\mu/(1+\alpha)$, with $\mu = 39.6$ GPa. Here kT is used as the unit of ΔG.

Load (μN)	μ (GPa)	G_I (GPa)	G_{II} (GPa)	$\beta\Omega$ (10^{-5} nm^3)	η (MPa s)	t_c (ms)	ΔG (kT)
400	–	33.4 ± 2.4	(6.2)	(1.89)	9.07 ± 1.40	0.32 ± 0.07	22.6 ± 0.3
600	–	34.1 ± 1.2	(5.5)	(1.63)	9.18 ± 1.11	0.34 ± 0.05	22.6 ± 0.2
800	–	32.4 ± 0.9	(7.2)	(2.29)	8.47 ± 0.95	0.29 ± 0.03	22.5 ± 0.1
1600	–	32.6 ± 0.6	(7.0)	(2.18)	8.24 ± 1.50	0.24 ± 0.04	22.3 ± 0.2
2000	39.7 ± 2.4	30.4 ± 0.3	9.3 ± 2.4	3.07 ± 0.61	22.9 ± 3.3	3.4 ± 0.9	24.9 ± 0.3
2400	39.5 ± 1.8	30.8 ± 0.3	8.7 ± 1.8	2.86 ± 0.45	20.5 ± 2.1	3.1 ± 0.5	24.8 ± 0.2
2800	40.0 ± 1.7	30.0 ± 0.3	10.0 ± 1.7	3.37 ± 0.42	23.9 ± 3.8	3.2 ± 0.3	24.9 ± 0.1
3200	39.6 ± 2.0	30.1 ± 0.2	9.5 ± 2.0	3.19 ± 0.51	24.5 ± 3.9	3.5 ± 0.7	24.9 ± 0.2
3600	39.4 ± 3.1	29.8 ± 0.3	9.6 ± 3.1	3.25 ± 0.75	23.4 ± 4.9	3.4 ± 0.9	24.9 ± 0.2
4000	39.5 ± 2.6	28.2 ± 0.3	11.3 ± 2.6	4.06 ± 0.65	32.2 ± 3.9	4.1 ± 0.6	25.1 ± 0.1

as shown in Fig. 2a. For comparison with the existing experimental data, a Zr-based MG with the nominal composition of $Zr_{52.5}Ti_5Cu_{17.9}Ni_{14.6}Al_{10}$ (Vit105) was selected as the model material. Prior to indentation, the amorphous structure of the sample was confirmed by the X-ray diffraction and differential scanning calorimetry (not shown) and the sample surface was mechanically polished to a mirror finish. The nanoindentation was subsequently performed on the TI 950 TriboIndenter system (Hysitron Inc., Minneapolis, MN) with a 5 μm spherical indenter at room temperature. During the experiments, indentations with the holding load, P_H, elevated from 400 to 4000 μN (as listed in Table 1), were carried out. In virtue of the ultrafast data acquisition capability (with a maximum of ~30,000 points per second) of the nanoindentation system, unusually high loading rates could be achieved. To reveal the effect of anelasticity, the loading time, t_L, was systematically varied from $\sim 10^0$ to $\sim 10^{-3}$ s. In all of these tests, the holding time, t_H, and unloading time, t_U, were both fixed at 0.1 s, which sufficed to allow for the full recovery of the anelastic deformation caused by the fast loading.

4. Results and discussions

4.1. Fitting of indentation load–displacement curve

Fig. 2b presents a set of nanoindentation load–displacement (P–h) curves acquired at $P_H = 3200$ μN. It is can be seen that all P–h curves return to the zero displacement after unloading, indicative of the elastic nature of the deformation. For slow indentations ($t_L > 0.036$ s), the loading and unloading curves overlap and obey the Hertzian theory; while for relatively fast indentations ($t_L < 0.036$ s), the loading curves depart from the Hertzian theory and the extent of departure increases with the decreasing t_L, which conforms to the character of an anelastic deformation. However, the anelastic deformation is fully relaxed during the holding period, and therefore all unloading curves collapse onto the same Hertzian solution. A similar phenomenon was observed for other indentation loads, ranging from 400 to 4000 μN. These experimental observations are consistent with the theoretical modeling.

Following the integral transform method [23,32] (see Appendix A), the loading curve of spherical indentation can be easily derived in line with the three-parameter viscoelastic model (Fig. 1d), which is $h(t)^{3/2} = \frac{3P(t)(1-\nu)}{8\sqrt{R}G_I} - \frac{3\dot{P}(1-\nu)G_{II}t_c}{8\sqrt{R}G_I(G_I+G_{II})}\left[1-\exp\left(-\frac{t}{t_c}\right)\right]$, where R denotes the indenter tip radius, ν the Poisson's ratio, $\dot{P}$ the loading rate and t_c the apparent relaxation time $t_c = \eta(G_I+G_{II})/(G_IG_{II}) = \exp[\Delta G/(kT)]/(2\omega)$. For simplicity, ν is assumed to be a constant in deriving the P–h relation for the three-parameter model. Through nonlinear data fitting, the three unknown viscoelastic properties, i.e. G_I, G_{II} and η, can be extracted from the experimental loading curves (see Appendix B). In turn, μ, t_c and $\beta\Omega$ can be obtained accordingly with $T = 293$ K (the ambient temperature). These fitted values are averaged at each indentation load and tabulated in Table 1.

Fig. 3a shows a comparison of the experimental and theoretical loading curves at $P_H = 3200$ μN, from which it can be seen that the model captures the experimental data very well. Here, it is worth mentioning that G_{II} and η at 400, 600, 800 and 1600 μN cannot be fitted directly using the three-parameter viscoelastic model. Instead, the viscoelastic behavior of the MG at these small loads is akin to the Kelvin model, which is the special form of Eq. (2) for $\dot{\tau} \sim 0$. Mechanistically, if the deformation in the spring G_{II} relaxes with time so fast that its presence cannot be detected experimentally, the spring G_{II} may be regarded as a rigid body, and thus the three-parameter model will degenerate to the Kelvin model. To facilitate the flow of discussion, the details of the model degeneration are discussed in Appendix B and are omitted here for brevity.

4.2. Invariant vs. variant shear modulus

Fig. 3b displays the variation of μ with the indentation load and loading time. Interestingly, the μs appear to be a constant regardless of the loading condition. By comparison, the obtained G_I stays very stable at ~33 GPa when the indentation loads are less than ~1600 μN, which is very close to the room-temperature shear modulus of Vit105 (31 GPa) measured by the ultrasonic method [8]. However,

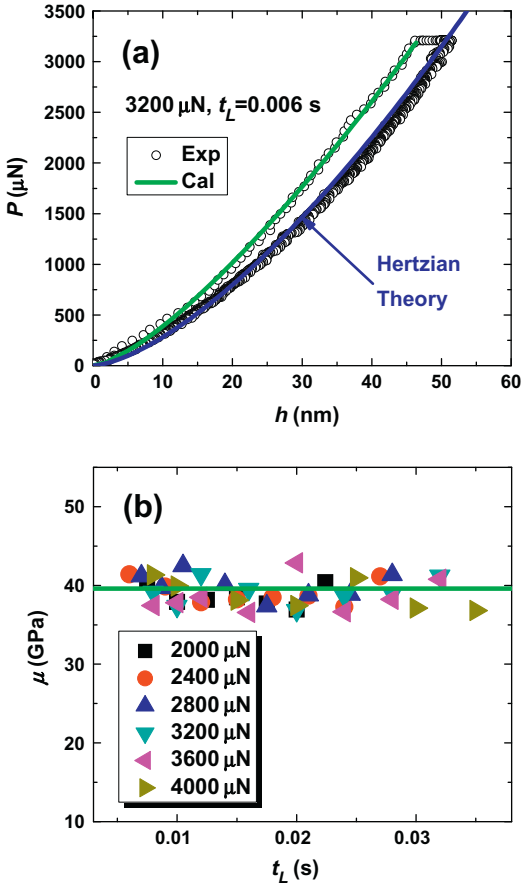

Fig. 3. (a) A typical comparison of the experimental (Exp) and calculated (Cal) loading curves for nanoindentation. Note that the Hertzian unloading curve gives the estimation of G_I. (b) Fitted μs at different indentation loads with the solid line indicating their average.

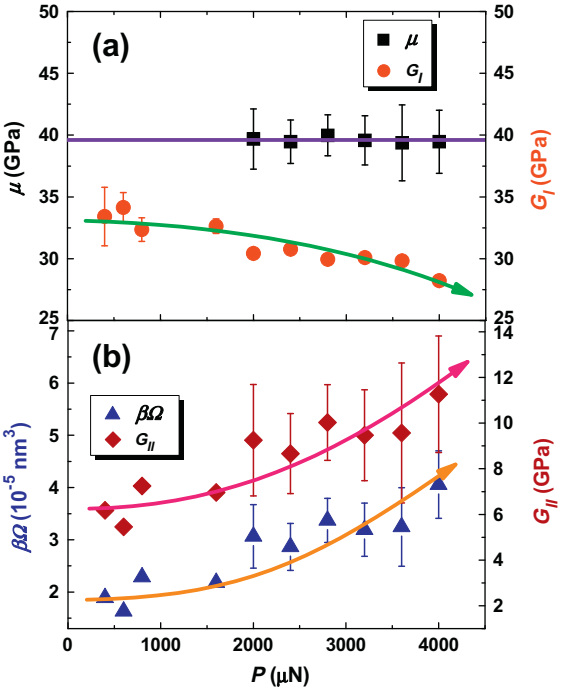

Fig. 4. (a and b) Variation of the obtained viscoelastic properties of the Vit105 MG with the indentation load. The arrowed trend lines are used here as a visual guide.

as the indentation load exceeds 1600 μN, G_I reduces as the indentation load rises. These findings imply that, during an "elastic" loading, the elastic matrix (shells) of the MG remains largely undamaged; however, the volume fraction of the liquid-like cores may still grow once the applied load reaches above a certain threshold even though this growth is limited and does not break down the elastic matrix of the amorphous structure.

As seen in Fig. 4a, μ attains the average value of ~39.6 GPa regardless of the indentation loads. This value is almost identical to the shear modulus (~39.2 GPa) of the devitrified MG, which can be estimated by taking the shear moduli of the constituent metallic elements [33] into the "rule of mixture" [8]. Note that this finding is consistent with our assumption that μ is the modulus derived from atomic bonding, which should be independent of the mechanical history of the alloy, and also with the results obtained by Cheng et al. through their atomistic simulations in 2009 [15]. On the other hand, the same finding can have an interesting implication for the maximum shear modulus attainable to a MG alloy. According to Eq. (4), G_I could increase if the liquid-like regions can be reduced, say, by thermal annealing; however, the maximum of G_I should be capped by the devitrification limit. Theoretically, this annealing effect can be presented as the curve of G_I vs. α^{-1}, as shown in Fig. 5a. Here the reciprocal of α is used such that the direction of the abscissa conforms to the time lapse in an isothermal annealing experiment. In Refs. [34,35], the shear modulus of the Vit1 MG was measured after thermal annealing to various degrees but with its amorphous structure being preserved [8]. As shown in Fig. 5b, the relative increase in the experimentally measured shear modulus increases with annealing time but it is capped by a limit of ~25%. Comparing Fig. 5a and b, it is evident that our model predicts this limit of modulus increase in excellent agreement with the available experimental data; meanwhile, it also yields the similar trend of the annealing effect despite the use of the different reference parameters, i.e. α^{-1} in Fig. 5a and the annealing time in Fig. 5b. Albeit qualitative, we believe that this similarity between the two trends (Fig. 5a and b) warrants future work that may deepen our understanding of the annealing effect on a quantitative basis.

4.3. Dynamics of structural evolution in apparent elastic regime

Next, let us discuss the stress-induced dynamics of the structural evolution that underpins the variation of G_I. As seen in Table 1, the activation energy, ΔG, against the local configurational transition in the liquid-like cores can be estimated, which is within the range of ~22–25 kT (~0.55–0.65 eV) according to our experiments. This level

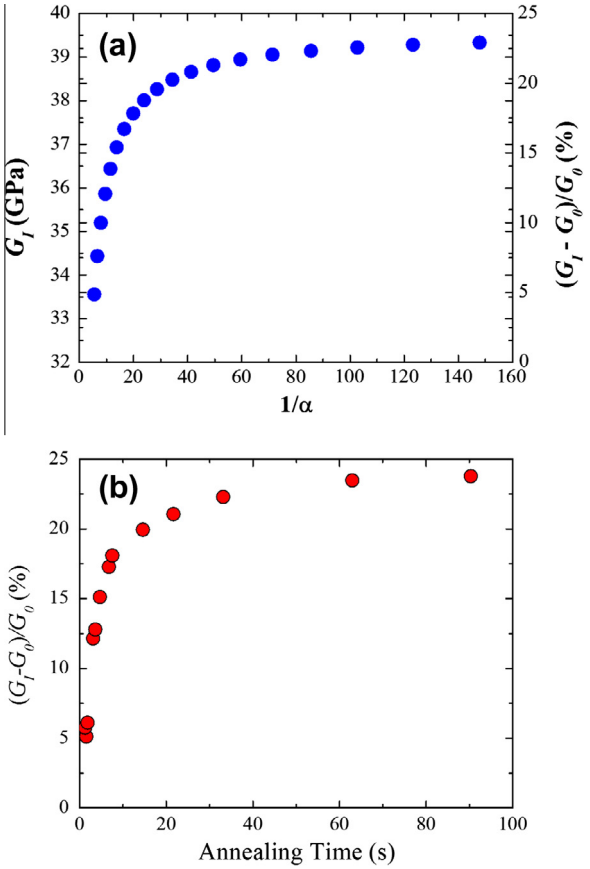

Fig. 5. (a) Variations of the G_I and the ratio $(G_I–G_0)/G_0$ with $1/\alpha$ predicted according to the relations $G_I = \mu/(1+\alpha)$ and $\mu = 39.6$ GPa (note that the reference modulus G_0 is here taken to be 32 GPa); and (b) the variation of the relative increase in G_I with annealing time experimentally measured for Vit1. The experimental data are taken from Ref. [8] and G_0 here denotes the shear modulus before thermal annealing.

of activation energy is comparable to that (~0.3–0.5 eV) of the internal friction measured for the Zr-based MGs in the temperature range of ~150–250 K [36], but lower than the activation energy against a typical STZ event (~$26kT_g$ or ~1 eV) as estimated using the cooperative shear model [37,38]. Note that the activation energy of a similar level (~0.5 eV) was also found experimentally by Schall et al. at room temperature for a single shear transformation (ST) event in the colloidal glass [39]. This suggests that, in contrast to the cooperative ST events one may encounter at the yielding point [37,38], the dynamic structural relaxation detected in this study is due to the activation of many single (or isolated) ST events homogeneously distributed within the sample volume during the apparent elastic deformation of the MG.

Aside from the activation energy, the variation in the activation volume can also be inferred from our experiments. However, only the combined term $\beta\Omega$ can be extracted herein. Since β measures the sensitivity of the total strain to its inelastic strain component, the higher its magnitude, the more liquid-like is the deformation behavior of the core–shell unit. As such, the variation in $\beta\Omega$ can reflect the change in the volume fraction of the activated liquid-like regions in the MG. As shown in Fig. 4b, at an indentation load less than 1600 μN, which corresponds to the mean shear stress of ~60% of the overall yielding stress, τ_y, of Vit105, $\beta\Omega$ fluctuates in the vicinity of 2×10^{-5} nm^3, implying an insignificant change in the volume fraction of the liquid-like cores. This activation process corresponds to a constant energy barrier $\Delta G \sim 22\,kT$, as shown in Table 1. By comparison, when the indentation load exceeds 1600 μN, ΔG rises to a higher level $\sim 25\,kT$ and, meanwhile the term $\beta\Omega$ starts to increase with the indentation load. These results suggest that the activation energy against the configurational transition in the liquid-like cores could be elevated as their volume fraction increases. To rationalize these results, there are two possible explanations. First, there could be a rather broad distribution of the energy barrier against the thermally activated processes, according to the molecular dynamics simulation of Rodney and Schuh [40]. In such a case, it is likely that most of the activation processes triggered at a low indentation load possess a low energy barrier, as opposed to these high-energy-barrier events triggered at a higher indentation load. As a result of these successive activation processes, the number of the activated liquid-like regions increases with the load. Alternatively, the rise of the energy barrier could be due to the expansion of the activated liquid-like cores. As seen in the recent atomic force microscopy (AFM) images [18,20,28], such as Fig. 6a, which shows the energy dissipation map obtained from a Zr–Ni MG thin film [20], there are no sharp boundaries that can separate different deformation regions in a MG alloy (the inset of Fig. 6a), in line with a continuous distribution of atomic packing in an amorphous structure. In that regard, it is possible that the atoms enveloping a liquid-like core, which behave elastically at a small load, can be turned to liquid-like after their local packing environment is destroyed at a high load (Fig. 6b). Consequently, this also raises the energy barrier against the subsequent local structural transition as well as the volume fraction of the liquid-like regions. Unfortunately, we are not sure at the moment which mechanism is responsible for our experimental finding, and it is also possible that both are active during our indentation test. Finally, we should emphasize that, given the limitation of our current work, we cannot further raise the indentation load beyond ~4000 μN, at which the corresponding mean indentation shear stress is ~750 MPa or ~$0.75\tau_y$. When the indentation load is above that value, displacement pop-in or shear instability appears, thus invalidating the mean-field modeling.

5. Effects of fast vs. slow dynamic relaxation

So far, our analyses and discussions have been based on the "core–shell" concept. Since both regions in MGs are structurally amorphous, one legitimate question would be why some regions behave as elastic shells while others as viscous cores. As mentioned earlier in the introduction,

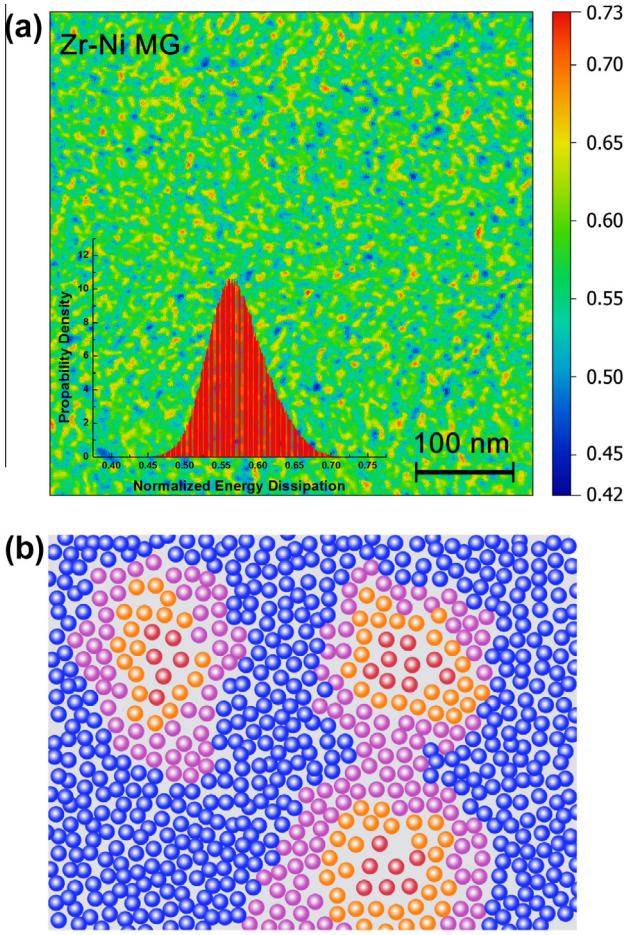

Fig. 6. (a) AFM structure image of the Zr–Ni MG thin film obtained through the mapping of anelastic energy dissipation (inset: the continuous distribution of the normalized energy dissipation). Note that the analysis of the AFM data is detailed in Ref. [20]. (b) Schematic illustration of the structural hierarchy around a liquid-like region (red sphere = loosely packed atom, orange sphere = less loosely packed atom, pink sphere = less densely packed atom, and blue sphere = densely packed atom). (For interpretation of the references to colour in this figure legend, the reader is referred to the web version of this article.)

the core–shell notion is more conceptual than physical and the distinction between the two kinds of regions is only an after-effect of mechanical deformation. According to Tanaka et al. [41], the phenomenon of glass transition is not only a dynamic slow-down of all constituent elements but also the percolation of "slow" regions in a supercooled liquid. If that was the case, the shell-regions we defined may be interpreted as those with a much longer relaxation time and thus higher viscosity than the core-regions. Therefore, they appear to be elastic simply because the external/experimental time scale is set much shorter than the internal/relaxation times of these regions.

Following this line of reasoning, one may naturally ask how one could distinguish a "quasi-static" process from a dynamic one given that there has been an increasing research interest recently in understanding the elastic behavior of MGs, particularly at the small length scale [42]. After all, the "elastic" shell could even flow at a small stress if one could wait for a long time. To address that

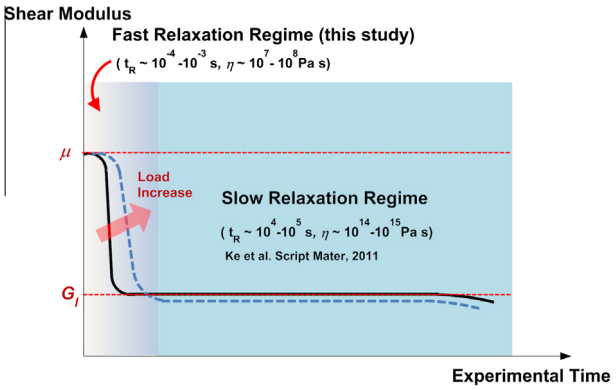

Fig. 7. Schematic illustration of the rate dependence of the shear modulus of a MG alloy in different relaxation regimes: fast relaxation leads to the rapid decay of the apparent shear modulus from μ to G_I within the time scale of 10^{-4}–10^{-3} s while the slow relaxation results in a slight decrease in G_I within the time scale of ~10 h [43]. Note that the trend of the rate dependence could be shifted by the external loading as shown by the dotted curve (e.g. Fig. 4a).

question, it is worth mentioning the creep tests performed by Ke et al. [43]. Their results show that, after loading a MG sample in its apparent elastic regime and waiting for tens of hours, there could be a very small (<1%) but detectable decrease in its quasi-static shear modulus. Based on the findings of Ke et al. [43] and the current study, we may draw a schematic (Fig. 7) showing the effects of the different dynamic relaxation processes on the apparent shear modulus of a MG, which could be determined readily from the slope of the linear portion of a stress–strain curve.

As shown in Fig. 7, for the case of an instant stepping load, the apparent shear modulus would appear to be μ, the one determined by the bonding strength in a MG; if the experimental time scale is within 10^{-4}–10^{-3} s, the apparent shear modulus decays rapidly from μ to G_I as a result of the configurational transition in the liquid-like cores, as seen in Fig. 2b. The resultant viscosity estimated from $\eta = t_R G_I$ would range from 10^7 to 10^8 Pa s in accord with this behavior of anelasticity. On the other hand, if the experimental time is set on the order of $\sim 10^5$ s, a slight decrease (<1%) in the quasi-static shear modulus could be witnessed due to the slow relaxation in the shell regions [43]. Similarly, the viscosity for the slow relaxation process could be also estimated, which is $\sim 10^{15}$ Pa s and 7–8 orders of magnitude higher than that for the fast relaxation process. In view of such a large discrepancy between the two extreme time scales, a quasi-static process is well defined in between, as is the case for most mechanical tests reported in the literature.

6. Summary

In summary, the structural origin of the shear modulus and the underlying structural evolution process in MGs is elucidated. Consistent with the notion of intrinsic structural heterogeneity in MGs, here we show that there are two concurrent contributions, i.e. bonding strength and

configurational transition (or fast dynamic relaxation), to their quasi-static shear modulus. The key findings of the current work are listed as follows:

(i) The shear modulus of a MG has two contributing terms: one is related to the atomic bonding (energy) and the other to the configurational transition of a glass (entropy). For the Vit105 MG, the energetic modulus (~40 GPa) is equivalent to the compositional average of the moduli of all constituent elements; while the configurational or entropic modulus (~6–10 GPa) varies with mechanical loads even in the elastic regime. The ratio of the two is ~15–25% and roughly equals the gap between the shear moduli of the amorphous and corresponding crystalline alloys [8].

(ii) The volume fraction of the activated liquid-like cores in the Vit105 MG increases remarkably only after the external load is increased above ~60% of the yielding load. Accordingly, the relaxation times and activation energies of the subcritical transition events are elevated from ~0.3 to ~3 ms, and ~0.55 to ~0.65 eV, respectively. Note that the activation energies are consistent with that estimated for a single ST event in a colloidal glass [39], and also with the early measurement of the internal friction in Zr-based MGs [36], but only half of the energy barrier (~1–2 eV) against cooperative ST events that lead to the overall yielding in MGs [37].

(iii) Our findings also indicate that the apparent shear modulus of a MG alloy is strongly time dependent in the fast relaxation regime (10^{-4}–10^{-3} s) and afterwards decays to its quasi-static value, which would remain stable until the MG alloy enters into the slow relaxation process on the time scale of ~10^5 s inferred from the prior data [43].

Finally, we would like to point out that, since the deformation heterogeneity as manifested by the solid- and liquid-like regions is not specific to MGs but also applicable to other amorphous materials, such as colloidal glasses [39], granular matters [44] and glassy polymers [45], the proposed theoretical and experimental framework is expected to be also useful for a wide range of amorphous materials of great technological importance.

Acknowledgements

This work was supported by MOST 973 of China (No. 2010CB731603) and the NSF of China (Nos. 50921091 and 51271195). The research of Y.Y. and C.T.L. is supported by the Research Grant Council (RGC), the Hong Kong Government, through the General Research Fund (GRF) with the grant number CityU530711 and CityU522110, respectively. Useful discussions with Z.Y. Liu, B.A. Sun and S.T. Liu are appreciated.

Appendix A. Derivation of time-dependent *P–h* relation

The *P–h* relation for an elastic contact in the spherical nanoindentations can be expressed by the Hertzian theory [23]:

$$h^{3/2} = \frac{3P(1-\nu)}{8\sqrt{R}G}, \tag{A1}$$

where R is the indenter tip radius, ν and G denote the Poisson's ratio and shear modulus of the material, respectively. According to the integral transform method [32], after the Laplace transform of the parameters in Eq. (A1), there is $\hat{h}^{3/2} = \frac{\widehat{3P(1-\nu)}}{8\sqrt{R}\widehat{G}}$, where $\hat{h}$, $\widehat{P}$ and $\widehat{G}$ are the Laplace-transformed displacement, load and shear modulus, respectively. Here we assume that the Poisson's ratio remains constant before and after the Laplace transform.

The Laplace-transformed shear modulus for the three-parameter anelastic model is expressed as:

$$\widehat{G} = (G_I + G_{II}) - \frac{G_{II}^2/\eta}{s + G_{II}/\eta}. \tag{A2}$$

Therefore,

$$\hat{h}^{3/2} = \frac{3\widehat{P}(1-\nu)}{8\sqrt{R}}A, \tag{A3}$$

where $A = \frac{1}{G_I+G_{II}}\left[1 + \frac{\frac{G_{II}^2}{\eta(G_I+G_{II})}}{s+\frac{G_I G_{II}}{\eta(G_I+G_{II})}}\right]$.

Applying the inverse Laplace transform, we have:

$$h^{3/2} = \frac{3(1-\nu)}{8\sqrt{R}(G_I+G_{II})}\left[P + \int_0^t P(\tau) f(t-\tau)d\tau\right], \tag{A4}$$

where $f(t) = \frac{1}{2\pi i}\int_{a-i\infty}^{a+i\infty} \frac{\frac{G_{II}^2}{\eta(G_I+G_{II})}}{s+\frac{G_I G_{II}}{\eta(G_I+G_{II})}} e^{st} \qquad ds = \frac{G_{II}^2}{\eta(G_I+G_{II})} e^{-\frac{t}{t_c}}$, and $t_c = \frac{\eta(G_I+G_{II})}{G_I G_{II}}$. As such, we obtain the *P–h* relation for the loading process of spherical nanoindentations for the anelastic material depicted by the mechanical model shown in Fig. 1d:

$$\begin{aligned} h^{3/2} &= \frac{3(1-\nu)}{8\sqrt{R}(G_I+G_{II})}\left[P + \frac{G_{II}^2}{\eta(G_I+G_{II})}\int_0^t P(\tau)e^{-\frac{t-\tau}{t_c}}d\tau\right] \\ &= \frac{3P(t)(1-\nu)}{8\sqrt{R}G_I} \\ &\quad - \frac{3\dot{P}(1-\nu)G_{II}t_c}{8\sqrt{R}G_I(G_I+G_{II})}\left[1-\exp\left(-\frac{t}{t_c}\right)\right]. \end{aligned} \tag{A5}$$

Appendix B. Data fitting and anelastic model degeneration

In slow indentations, such as $t_L > 0.036$ s in Fig. 2b, the second term on the right-hand side of Eq. (A5), which is closely related to the liquid-like cores, is small and can be neglected. Consequently, the *P–h* relation recovers to the Hertzian solution, i.e. $h(t)^{3/2} = 3P(t)(1-\nu)/(8G_I R^{1/2})$, as consistent with our experimental results. Thus G_I can be

firstly obtained via fitting the loading curves in slow indentations. For each load, at least 10 loading curves with $t_L \geqslant 0.1$ s were fitted and the average value is listed in Table 1. With the known G_I, then G_{II} and η at each load above 1600 μN were extracted by fitting the loading curves that deviate significantly from the unloading curves with Eq. (A5). The other parameters for each indentation with $P_H > 1600$ μN, i.e. μ, t_c and $\beta\Omega$, were then computed according to $G_I = \mu - G_{II}$, $t_c = \eta(G_I + G_{II})/(G_I G_{II})$ and $G_I = \mu/(1+\alpha)$, respectively, with $T = 293$ K.

When fitting the anelastic indentation curves with $P_H \leqslant 1600$ μN using the three-parameter model, the fitted G_{II}'s tend to be infinitely large, implying that the three-parameter model degenerates to the Kelvin model (presented in Fig. B1a) at these low indentation loads. To explain this, it needs to be remembered that the three-parameter model (Eq. (2)) is derived by assuming that the external stress could be ramped up with time in a continuous manner. However, in real mechanical tests, the applied load always steps up incrementally. As illustrated in Fig. B1b, there is a time interval, t_S, before each load increment can be added to the material. The maximum data acquisition rate of our indentation system (30,000 points per second) sets the limit of 0.033 ms for t_S.

As shown in Fig. B1b, when an stress increment, $\Delta\tau$, is exerted onto the three-parameter model at the time t_0, an instantaneous strain increase, $\Delta\gamma_0$, will be produced in the spring G_I and G_{II}, and, therefore, we could have $\Delta\tau = \Delta\gamma_0(G_I + G_{II})$ at $t = t_0$. However, as the time lapses ($t_0 < t < t_0 + t_S$), the dashpot starts to deform and hence the strains in the springs are redistributed. Keeping $\Delta\tau$ to be a constant, we have:

$$\Delta\tau = \Delta\gamma \cdot G_I + \Delta\tau_2, \tag{B1}$$

where $\Delta\gamma$ is the strain increment in the whole model after relaxation, and $\Delta\tau_2$ is the stress increment born by the Maxwell unit:

$$\Delta\tau_2 = \eta \cdot \frac{d(\Delta\gamma_\eta)}{dt} = \Delta\gamma_{II} \cdot G_{II}, \tag{B2}$$

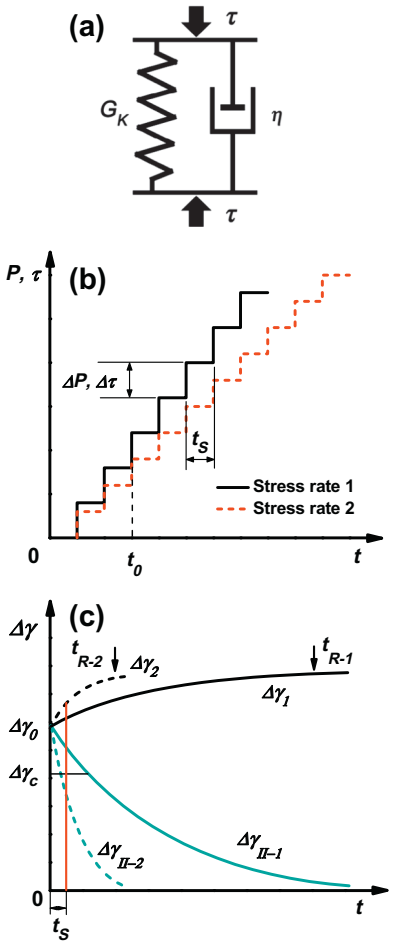

Fig. B1. (a) Sketch of the Kelvin model, (b) schematic illustration of the discrete load stepping process (t_S is the time lapse for the indentation system to execute one load increment ΔP (or one stress increment $\Delta\tau$)), and (c) illustrated variations of $\Delta\gamma$ and $\Delta\gamma_{II}$ with time for the cases of a high indentation load ($P_H > 1600$ μN, the solid lines) and a low indentation load ($P_H \leqslant 1600$ μN, the dashed lines). The arrows indicate the times, $t_{R\text{-}1}$ and $t_{R\text{-}2}$, for the full recovery of the anelastic deformation in the above two cases, respectively.

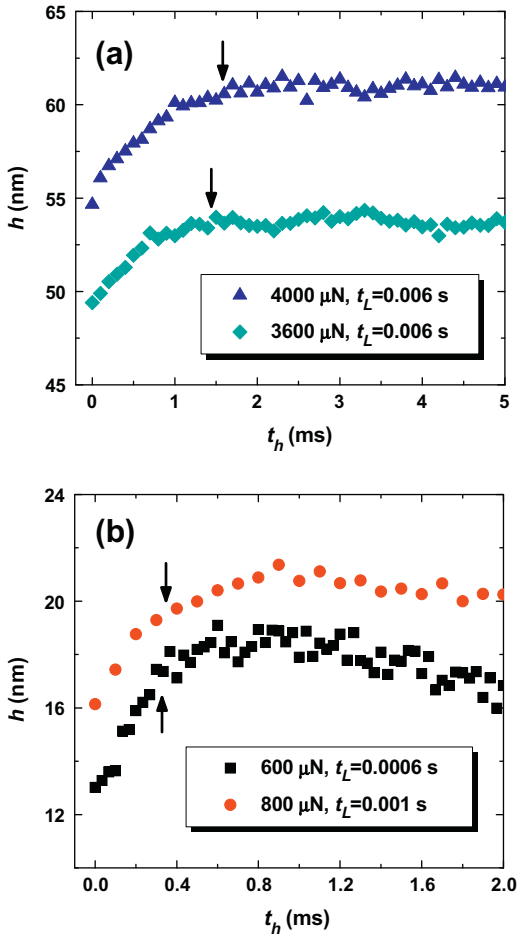

Fig. B2. The recovery of the anelastic deformation of the Vit105 MG as measured during the holding process at (a) $P_H = 3600$ and 4000 μN, and (b) $P_H = 600$ and 800 μN. t_h is the holding time and the arrows mark the full recovery of the anelastic deformation.

where $\Delta\gamma_\eta$ and $\Delta\gamma_{II}$ are respectively the strain increment in the dashpot and spring G_{II}. Combining Eqs. (B1) and (B2), we obtain:

$$\frac{d(\Delta\gamma_{II})}{dt} = -\frac{G_I}{G_{II}} \cdot \frac{d(\Delta\gamma)}{dt}, \tag{B3}$$

which gives the relation between the time rates of the change of the strain increment in the whole model and that in the spring G_{II} during each load stepping.

As mentioned in Section 4.1, the anelastic deformation exhibited during the fast loading can be fully relaxed after the holding process. Fig. B2a and b displays the recovery of the anelastic deformation in the MG for the holding time $t_H = 0.1$ s at different load levels. From these curves, it is clear that the time (t_R), which the MG needs for a full recovery at a constant load, is ~1.5 ms at the high loads and ~0.3 ms at the lower loads. According to the fitting results, the ratio of G_I/G_{II} ranges from 3 to 5. Therefore, it can be inferred from Eq. (B3) that the strain in the spring G_{II} decays very fast and the rate is about 3–5 times that for the strain increase in the spring G_I. Note that the nanoindenter only records the displacement at the end of each load increment. Hence, when $\Delta\gamma_{II}$ diminishes to a level below the resolution of the testing machine, $\Delta\gamma_c$, the strain in the spring G_{II} cannot be detected experimentally. In other words, the material appears to behave as a Kelvin model due to the fast decay of the strain in the spring G_{II}. To illustrate this idea, Fig. B1c presents a schematic about the variations of $\Delta\gamma$ and $\Delta\gamma_{II}$ with time for the case of a high and low indentation load. As shown by this figure, given the same machine limits $\Delta\gamma_c$ and t_s, the presence of the spring G_{II} is more likely to be revealed at a high indentation load and a large relaxation time than at a low indentation load and a small relaxation time.

According to the Kelvin model, the P–h relation for spherical indentation is given below [23]:

$$h(t)^{3/2} = \frac{3P(t)(1-\nu)}{8\sqrt{R}G_K} - \frac{3\dot{P}(1-\nu)t_c}{8\sqrt{R}G_K}\left[1 - \exp\left(-\frac{t}{t_c}\right)\right], \tag{B4}$$

where G_K ($\approx G_I$) denotes the shear modulus of the spring, and $t_c = \eta/G_K$. Using Eq. (B4), η and t_c could be backed out by fitting the fast-rate loading curves, and their averaged values are listed in Table 1. Similarly, t_c in the Kelvin model can be related to the energy barrier and attempt frequency [29] through $t_c = \exp[\Delta G/(kT)]/(2\omega)$. Since these subcritical activation events are rather localized [29], Ω should be on the order of an atomic volume and thus ω be close to the Debye frequency (~10^{13} Hz). With these considerations, different ΔG's can be computed according to $t_c = \exp[\Delta G/(kT)]/(2\omega)$ and their averaged values are also shown in Table 1.

References

[1] Greer AL. Science 1995;267:1947.
[2] Löffler JF. Intermetallics 2003;11:529.
[3] Wang WH. Adv Mater 2009;21:4524.
[4] Takeuchi S, Edagawa K. Prog Mater Sci 2011;56:785.
[5] Greer AL, Ma E. MRS Bull 2007;32:611.
[6] Busch R, Schroers J, Wang WH. MRS Bull 2007;32:620.
[7] Wang WH. J Appl Phys 2006;99:093506.
[8] Wang WH. Prog Mater Sci 2012;57:487.
[9] Golding B, Bagley BG, Hsu FSL. Phys Rev Lett 1972;29:68.
[10] Zhao ZF, Zhang Z, Wen P, Pan MX, Zhao DQ, Wang WH, et al. Appl Phys Lett 2003;82:4699.
[11] Safarik DJ, Schwarz RB. Acta Mater 2007;55:5736.
[12] Ma D, Stoica AD, Wang X-L, Lu ZP, Clausen B, Brown DW. Phys Rev Lett 2012;108:085501.
[13] Cheng YQ, Ma E. Phys Rev B 2009;80:064104.
[14] Leonforte F, Boissiere R, Tanguy A, Wittmer JP, Barrat J-L. Phys Rev B 2005;72:224206.
[15] Cheng YQ, Cao AJ, Ma E. Acta Mater 2009;57:3253.
[16] Park KW, Lee CM, Wakeda M, Shibutani Y, Falk ML, Lee JC. Acta Mater 2008;56:5440.
[17] Dmowski W, Iwashita T, Chuang CP, Almer J, Egami T. Phys Rev Lett 2010;105:205502.
[18] Liu YH, Wang D, Nakajima K, Zhang W, Hirata A, Nishi T, et al. Phys Rev Lett 2011;106:125504.
[19] Ye JC, Lu J, Liu CT, Wang Q, Yang Y. Nat Mater 2010;9:619.
[20] Yang Y, Zeng JF, Liu CT, Volland A, Blandin JJ, Gravier S. Acta Mater 2012;60:5260.
[21] Fujita T, Wang Z, Liu YH, Sheng H, Wang WH, Chen MW. Acta Mater 2012;60:3741.
[22] Concustell A, Sort J, Greer AL, Baro MD. Appl Phys Lett 2006;88:171911.
[23] Yang Y, Zeng JF, Ye JC, Lu J. Appl Phys Lett 2010;97:261905.
[24] Caron A, Kawashima A, Fecht HJ, Louzguine-Luzguin DV, Inoue A. Appl Phys Lett 2011;99:171907.
[25] Huo LS, Ma J, Ke HB, Bai HY, Zhao DQ, Wang WH. J Appl Phys 2012;111:113522.
[26] Argon AS. Acta Metall 1979;27:47.
[27] Fan C, Liaw PK, Liu CT. Intermetallics 2009;17:86.
[28] Wagner H, Bedorf D, Kuchemann S, Schwabe M, Zhang B, Arnold W, et al. Nat Mater 2011;10:439.
[29] Liu ZY, Yang Y. Intermetallics 2012;26:86.
[30] Flügge W. Viscoelasticity. Berlin: Springer-Verlag; 1975.
[31] Dyre JC. Rev Mod Phys 2006;78:953.
[32] Christensen RM. Theory of viscoelasticity. New York: Dover Publications; 2003.
[33] Gale WF, Totemeir TC. Simthells metals reference book. Oxford: Elsevier Butterworth-Heinemann Ltd.; 2004.
[34] Wang WH, Li LL, Pan MX, Wang RJ. Phys Rev B 2001;63:052204.
[35] Wang WH, Wang RJ, Yang WT, Wei BC, Wen P, Zhao DQ, et al. J Mater Res 2002;17:1385.
[36] Khonik VA, Spivak LV. Acta Mater 1996;44:367.
[37] Johnson WL, Samwer K. Phys Rev Lett 2005;95:195501.
[38] Yu HB, Wang WH, Bai HY, Wu Y, Chen MW. Phys Rev B 2010;81:220201.
[39] Schall P, Weitz DA, Spaepen F. Science 2007;318:1895.
[40] Rodney D, Schuh C. Phys Rev Lett 2009;102:235503.
[41] Tanaka H, Kawasaki T, Shintani H, Watanabe K. Nat Mater 2010;9:324.
[42] Tian L, Cheng Y-Q, Shan Z-W, Li J, Wang C-C, Han X-D, et al. Nat Commun 2012;3:609.
[43] Ke HB, Wen P, Peng HL, Wang WH, Greer AL. Scripta Mater 2011;64:966.
[44] Richard P, Nicodemi M, Delannay R, Ribiere P, Bideau D. Nat Mater 2005;4:121.
[45] Ward IM, Sweeney J. An introduction to the mechanical properties of solid polymers. New York: John Wiley; 2008.